## RESEARCH ARTICLE

# Conformal Transformation Analysis of Capacitive Wireless Charging

**HUSSEIN MAHDI**, (Graduate Student Member, IEEE),
**BJARTE HOFF**, (Senior Member, IEEE), **PÅL GUNNAR ELLINGSEN**,
**AND TROND ØSTREM**, (Member, IEEE)
Department of Electrical Engineering, UiT–The Arctic University of Norway, 8514 Narvik, Norway
Corresponding author: Hussein Mahdi (hussein.al-sallami@uit.no)

**ABSTRACT** This paper studies the capacitive coupling in a capacitive power transfer (CPT) system designed for charging applications. It proposes mathematical models using the conformal transformation for calculating air-gapped and underwater capacitance and verifies the proposed models using COMSOL multiphysics and measurements. The measured results show that we can achieve nano-farad capacitance ranges if we submerge the capacitor in seawater. The seawater's capacitance slightly changes when we increase the gap distance or the operating frequency. As the under seawater CPT system can be an attractive option for loosely-coupled charging applications, we further examine the system by focusing on the cross-coupling effects. The results show that the cross-coupling between the plate degrades the system's power transfer capability and efficiency. With negligible cross-coupling effects, the system gives 129 W output power at an efficiency of 81.2%.

**INDEX TERMS** Wireless power transmission, capacitive power transfer, couplings, energy efficiency, conformal mapping, network theory.

## I. INTRODUCTION

Wireless power transfer (WPT) utilizes electromagnetic fields to transfer power between a transmitter and a receiver (couplers) without mechanical contact. It has emerged in high-power charging applications providing safe and convenient solutions. In such applications, the standard practice is to use near-field WPT in which the distance between the couplers is much shorter than the wavelength of the electromagnetic fields. Near-field WPT comprises two main groups: inductive and capacitive power transfer.

Inductive power transfer (IPT) carries the power between the inductive couplers using magnetic fields. IPT is the most commonly used technique in high-power charging [1], as it provides the convenience of automatic charging through three modes: static, quasi-dynamic, and dynamic [2]. Thus, it has begun to receive attention for electric cars, buses, and trains charging applications [3].

The associate editor coordinating the review of this manuscript and approving it for publication was Kaigui Bian.

IPT suffers from eddy-current losses in the nearby metal, causing temperature rise problems [4]. Additionally, it contains expensive and heavy parts. As an alternative, capacitive power transfer (CPT) provides a cheaper and lighter solution than IPT using alternating electric fields. In the literature, many papers have proposed CPT charging on-road electric vehicles [5], [6], electric ships [7], [8], [9], and autonomous underwater vehicles [10], [11], [12].

Three performance metrics affect the overall system performance: the operating frequency of the system, the voltage across the capacitive couplers, and the coupling capacitance [7]. Decreasing the transfer distance, increasing the operating frequency, or increasing the voltage across the capacitors can enhance the power transfer of the system [12]. While safety regulations limit the operating frequency and voltage, we can improve the capacitance between the couplers.

The air-gapped capacitance is in the pico-farad (pF) range which limits the power transfer capability of the CPT system [5], [6]. One way to improve the coupling capacitance is

by decreasing the separation distance between the couplers or increasing the couplers' dimensions, but in both ways, we limit the applications of the CPT systems. Another way is by increasing the electrical permittivity of the medium between the couplers.

In electrical vehicle charging applications, researchers have tried inserting a layer of material with a high dielectric between the couplers instead of air to enhance the coupler's capacitance. For instance, Sakai *et al.* [13] proposed a CPT system through the road surface and the vehicle wheels utilizing steel belts in tires to overcome the short field-reachable range. Another approach by Yi [14] used the vehicle's windows to trap the electric fields for the coupling. In contrast, Dai and Ludois [15] transferred power through a flexible and compressive bumper that molds and contours itself to the vehicle to minimize the air gap and confine the field during charging.

Submerging the couplers in fresh- or seawater enhances the coupling and makes the CPT system more attractive for charging ships and underwater vehicles. In [9], the study analyzed the underwater CPT system using the finite element method (FEM) at a high frequency (HF) range. Similarly, other studies investigated the capacitive coupling at a short separation distance (up to 20 mm) in freshwater [10] and seawater [11], [12] at a MHz frequency range. The capacitor's behavior at the frequency range below the MHz range has received less attention.

This paper investigates the admittance of an air-gapped capacitor and capacitors submerged in fresh- and seawater. The investigation is carried out over 100 kHz to 1 MHz frequency range and 10 mm to 500 mm separation distances. We analyze the capacitance using a conformal transformation approach to consider the fringing effect. We propose mathematical models to calculate the capacitance of the air-gapped and underwater couplers. Moreover, we explain how we can consider the two-port $\pi$ model as a conformal transformation in the complex domain. Finally, we investigate the effect of cross-coupling on the power transferability and efficiency under seawater CPT systems.

We arrange the rest of the paper as follows: Section II investigates the fringing effect on the capacitance of the coupling plates in air and underwater. It also proposes analytical models based on the conformal transformation analysis. Section III presents the two-port model and explains how we can consider this model as a conformal transformation in the complex domain. In section IV, we verify the proposed analytical models using numerical analysis and experimental results. Then, we examine in detail the effect of the cross-coupling admittance on the under seawater CPT system's power transferability and efficiency in section V. Finally, we conclude in section VI.

## II. FRINGING EFFECT
Using a simplified electrostatic approximation model, we can approximate capacitance of the plates (coupling plates) as

$$C_0 = \frac{\kappa \epsilon_0 A}{d}, \qquad (1)$$

**TABLE 1.** Capacitance models considering fringing effects.

| Model | Formula | Shape |
|---|---|---|
| Simplified | $C_0 = \frac{\kappa A}{d}$ | General |
| Ignatius's 1932 [18] | $C = C_0[1 + \frac{2d}{\pi R} \ln(\frac{32R}{ed})]$ | Disc |
| Palmer 1937 [17] | $C = C_0[1 + \frac{d}{\pi L} \ln(\frac{2\pi L}{d})]^2$ | Square |
| Cooke 1958 [18] | $C = C_0[1 + \frac{2d}{\pi R} \ln(\frac{\pi e R}{d})]$ | Disc |
| Huston 1963 [18] | $C = C_0[1 + \frac{2d}{\pi R} \ln(\frac{8\pi R}{ed})]$ | Disc |
| Nishiyama 1994 [19] | $C = C_0(1 + 2.343b^{0.992})$ | Square |

where $\kappa$ is the dielectric constant, $\epsilon_0$ (C/V $\cdot$ m) is the permittivity of the free space, $A$ (m$^2$) is the area of the plates, and $d$ (m) is the distance between the plates.

In this model, assumptions are a uniform charge density distribution on the plates and negligible fringing fields at the edges. However, these assumptions are only valid when the aspect ratio ($b$), given by

$$b = \frac{\text{electrode distance}}{\text{electrode width}}, \qquad (2)$$

is very close to zero [16]. The assumptions fail when the charge density at the edges of the plates is more extensive than at the center. The electric fields near the edges of the plates are weaker than between them due to the fringing effect, which is the bending of electric field lines near the edges. Thus, the total capacitance of the plates increases because of the non-uniform distribution of fields near the edges.

### A. THE FRINGING EFFECT IN AIR
Although we might know the total charge on the plates, it is not easy to calculate the total charge density because of the non-uniform distribution of charges. We can attribute the non-uniformity to the induced charge densities on nearby conductors or polarization of dielectric material. Conformal transformation and the finite element method (FEM) are two approaches that can deal with the boundary problem. While the FEM approach might require expensive software to calculate the capacitance numerically, the conformal transformation can be a cheaper alternative.

Palmer [17] derived an analytical model using the conformal transformation approach for square-shaped plates. Sloggett *et al.* [18] also used the conformal transformation approach to study the fringing capacitance for a disc-shaped capacitor. In contrast, Nishiyama and Nakamura [19] proposed a numerical model using the boundary element method to derive the capacitance of square and rectangular plates. Table 1 lists some of the proposed models for both square- and disc-shaped plates.

We can apply the disc plates' models for square ones by assuming that the area of the disc electrode equals the area of the squared one.

$$A = L^2 = \pi R^2, \qquad (3)$$

where $L$ is the length of the edges of the square electrode and $R$ is the radius of the disc.
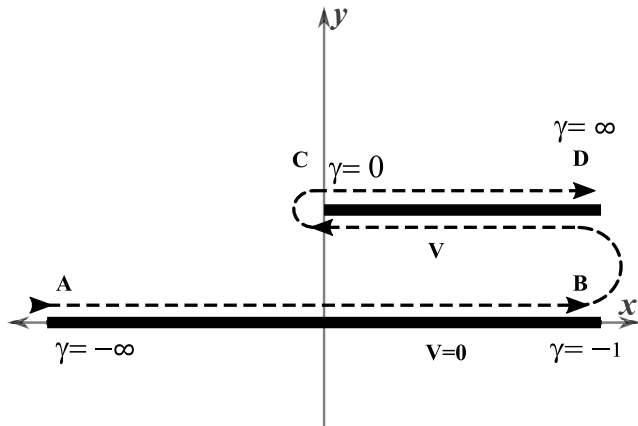
**FIGURE 1.** Illustration of the Schwartz-Christoffel transformation for the plates.

The conformal transformation approach uses complex conjugate functions to solve two-dimensional problems. According to [20], the theorem of Schwartz-Christoffel is a conformal mapping technique that transforms any polygon bounded by straight lines in the $z$-plane, where $z = x + jy$, into the real axis $\alpha$ of a new $\gamma$-plane, where $\gamma = \alpha + j\beta$. We can express the Schwartz-Christoffel transformation as [20]

$$\frac{dz}{d\gamma} = k \prod_{i=1}^{n} (\gamma - \gamma_i)^{a_i/\pi - 1}, \tag{4}$$

where $a_i$ are the internal angles of the polygon in the $z$-plane, $k$ is a constant and $\gamma_i$ are points on the real axis in $\gamma$-plane that correspond to the angular points of the polygon in the $z$-plane. The $a_1, a_2, \ldots, a_n$ in (4) are given values, while we can arbitrarily assume the constants $\gamma_1, \gamma_2, \ldots, \gamma_n$.

The value of $dz/d\gamma$ ($|dz/d\gamma|$) in (4) is either infinite or zero at the angles of the polygon. In contrast, $|dz/d\gamma|$ cannot vanish or become infinite for the area bounded by the real axis ($\alpha$-axis) and infinite semi-circle in the $\gamma$-plane. This area corresponds to the area bounded by the polygon in the $z$-plane. If the boundaries of the plates are considered the side of the polygon, then (4) transfer these lines into the real axis in the $\gamma$-plane.

Let $\phi$ be the potential function and $\psi$ be the electric field function, where $\omega = \phi + j\psi$, are conjugate functions that each solve Laplace's equation ($\nabla^2 \phi = 0$). A point in the boundary of the plate in $z$-plane corresponds to a point on the real axis in the $\gamma$-plane, and a line constant potential in the $\omega$-plane.

Fig. 1 illustrates the successive Schwartz-Christoffel transformation of the plates in three planes: $z$-plane, $\gamma$-plane, and $\omega$-plane. The upper electrode (CD) is assumed to be a semi-infinite plane with a potential function ($\phi = V$) in parallel to the electrode (AB) in an infinite plane with a potential function ($\phi = 0$). The sides of the plates describe the polygon (ABCD) as a dashed line in the direction of the arrows. The surfaces of the plates are straight lines stretching from $x = -\infty$ on the AB electrode to $x = \infty$ on the CD electrode in the $z$-plane.

In the $z$-plane, if a point travels over a straight line parallel to the $y$-axis, then the point moves around a semi-circle in the $\gamma$-plane, as (4) implies. Thus, the polygon consists of the two arc lines at the plates' edges. In the $\gamma$-plane, we arbitrarily select the values of $\gamma$ to be $\gamma = -1$ corresponding to the corner at B and $\gamma = 0$ corresponding to the corner at C. The internal angles of the polygon are zero at B and $2\pi$ at C. By substituting the values of $\gamma$ and the corresponding angles in (4), it gives

$$\frac{dz}{d\gamma} = k_1 \frac{\gamma}{\gamma + 1}, \tag{5}$$

where $k_1$ is a constant. When the polygon passes through $\gamma = -1$, then the value of $y$ increases $k_1 \pi$ and hence $y = d = k_1 \pi$, where d is the separation distance.

The $\omega$-plane only consists two lines, V and zero, as shown in Fig. 1. The internal angle at $\gamma = -1$ is zero. Thus, the transformation of $\omega$-plane to a real axis in the $\gamma$-plane can be expressed as

$$\frac{d\omega}{d\gamma} = k_2 \frac{1}{\gamma + 1}, \tag{6}$$

where $k_2$ is a constant.

When the polygon passes through $\gamma = -1$, then the value of $y$ decreases $k_2 \pi$, that is, $y = V = -k_2 \pi$. Solving (5) and (6) give

$$z = \frac{d}{\pi} [1 + \gamma - \ln(1 + \gamma) + j\pi] \tag{7a}$$

$$w = -\frac{V}{\pi} [\ln(1 + \gamma) - j\pi] \tag{7b}$$

From (7a), the real part of the $z$-plane can be written as

$$x = \frac{d}{\pi} [1 + \gamma - \ln(1 + \gamma)] \tag{8}$$

The surface charge density $\sigma$ can be expressed as

$$\sigma = \pm \frac{1}{4\pi} \frac{d\psi}{dy} = \pm \frac{1}{4\pi} \frac{d\phi}{dx} \tag{9}$$

Now, we can calculate the surface charge density for the upper surface and the lower surface of the CD plate. Starting with the lower surface, as the values of $\gamma$ ranges from $-1$ to zero, then we can simplify $\gamma$ from (8) as

$$\gamma = \frac{\pi x}{d} \tag{10}$$

From (7b), (9), and (10), we can express the charge density of the lower surface from zero to $\gamma$, in the $\gamma$-plane, as

$$\int \sigma \, da = \frac{1}{4\pi} [\phi(\gamma) - \phi(0)] = -\frac{V}{4\pi^2} [\ln(1 + \gamma)]$$
$$\approx \frac{V}{4\pi^2} (1 + \gamma) = \frac{V}{4\pi d} \left( x + \frac{d}{\pi} \right), \tag{11}$$

where $da$ is an element of the section of the conductor.

The charge density on the lower part of the electrode equals the uniform charge distribution on an infinite electrode that its width increases by a factor ($d/\pi$).

For the upper surface, as the values of $\gamma$ ranges from zero to infinity, then we can simplify $\gamma$ from (8) as

$$\gamma = \left[\frac{\pi x}{d} + \ln(1 + \frac{\pi x}{d})\right] \quad (12)$$

Similarly from (7b), (9), and (12), the surface charge density of the upper surface of the electrode is

$$\int \sigma \, da = \frac{1}{4\pi}[\phi(0) - \phi(\gamma)] = -\frac{V}{4\pi^2}[\ln(1 + \gamma)]$$

$$\approx \frac{V}{4\pi^2}\left\{\ln\left[1 + \frac{\pi x}{d} + \ln\left(1 + \frac{\pi x}{d}\right)\right]\right\} \quad (13)$$

The total charge surface density is the algebraic summation of the charge density on the upper and the lower surfaces. If the width of the plate is not semi-infinite, that is $x = L$, then the capacitance because of the fringing can be expressed as

$$C_f = \frac{\epsilon_0}{4\pi}\left\{1 + \frac{\pi L}{d} + \ln\left[1 + \frac{\pi L}{d} + \frac{1}{\pi}\ln\left(1 + \frac{\pi L}{d}\right)\right]\right\} \quad (14)$$

We can physically interpret the fringing capacitance as a capacitor that is connected in parallel with the capacitor of a uniform charge distribution on the plates, which is given in (1). Thus, we express the total capacitive of the air-gapped coupler as:

$$C = C_0 + C_f = \frac{\epsilon_0 L^2}{d}$$
$$+ \frac{\epsilon_0}{4\pi}\left\{1 + \frac{\pi L}{d} + \ln\left[1 + \frac{\pi L}{d} + \frac{1}{\pi}\ln\left(1 + \frac{\pi L}{d}\right)\right]\right\} \quad (15)$$

### B. THE FRINGING EFFECT IN WATER
Taking the electrical properties of water into consideration, we can write (6) as

$$\frac{d\omega}{d\gamma} = k_2 \frac{1}{\gamma + a}, \quad (16)$$

where the factor $a$ represents the conductivity effect of water and we can assume it to be $a = \pi^2/x$. From Fig. 1, if we neglect the surface charge density of the upper surface of the plates, due to the higher concentration of charges between the coupling plates in comparison with upper surfaces. Then we can express the charge density of the plates equals the charge on the lower surface as

$$\int \sigma \, da \approx \frac{V}{4\pi d}\left(x + \frac{\pi d}{x}\right) \quad (17)$$

The charge density equals the uniform charge distribution on an infinite plate whose width increases by a factor $(\pi d/L)$. Similar to (15), we can approximate the total capacitance in water as:

$$C \approx \frac{\kappa \epsilon_0 L^2}{d} + \frac{\kappa \epsilon_0}{4\pi d}\left(L + \frac{\pi d}{L}\right) \quad (18)$$
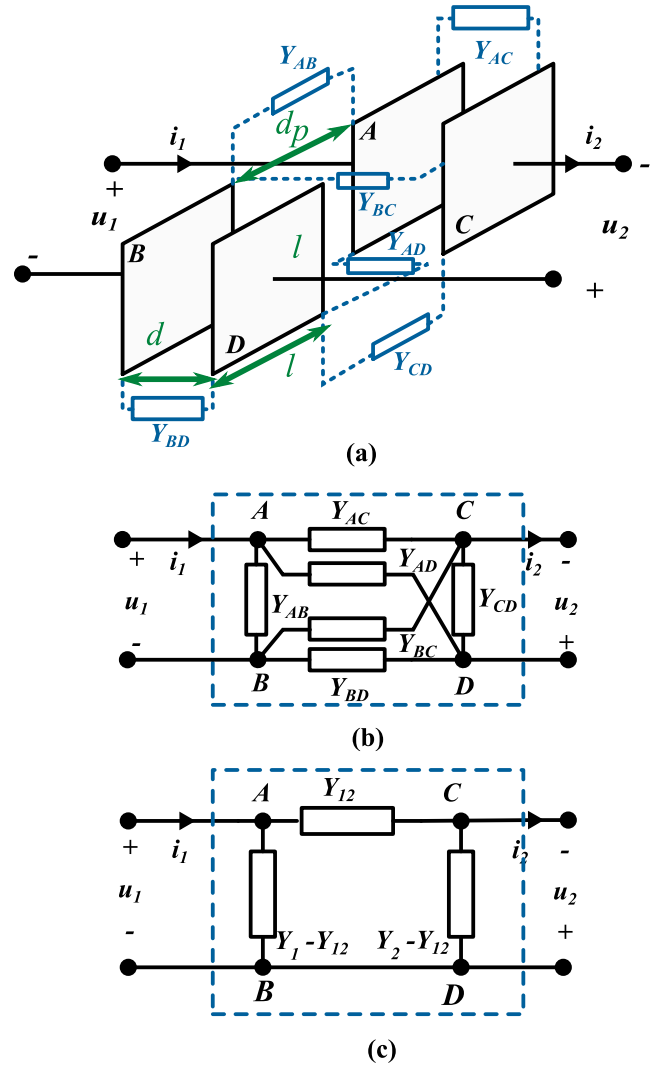


**FIGURE 2.** Model of the plate coupling: (a) The coupling between the four plates structures. (b) The circuit model of coupling admittance between the plates. (c) The $\pi$ model.

## III. TWO-PORT MODEL
The coupling between plates depends on the dimension of the plates and the medium's characteristics between the plates, as shown in (15) and (18). In the case of the air-gapped CPT system, we can neglect the air's conductivity and use the capacitors as circuit elements to represent the coupling between the plates. While in the case of an underwater CPT system, we cannot neglect the water's conductivity due to the presence of the dissolved ions in the water; hence, we represent the conductivity of the water by the conductance. As a general case, we can principally use the admittance to model the coupling between the plates in a CPT as

$$Y = G + jB, \quad (19)$$

where $G$ is the conductance of the medium and $B$ is the susceptance between the plates.

Fig. 2(a) shows four plates (A, B, C, and D) which are a simple CPT structure where the plates (B and D) generate

a return path for the resonant current. The admittance $Y_{AC}$ and $Y_{BD}$ are the mutual coupling between the plates. While the admittance $Y_{AD}$ and $Y_{BC}$ are the cross-coupling between the plates. Finally, the admittance $Y_{AB}$ and $Y_{CD}$ are the self-coupling between the plates, as illustrated in Fig. 2(b).

The mutual and cross coupling form a general lattice network which is unstable due to the inevitable interaction between the elements of the network. We can simplify in to a $\pi$-network whose elements are [21]

$$Y_{ab} = \frac{(Y_{AC} + Y_{AD}) \cdot (Y_{BC} + Y_{BD})}{(Y_{AC} + Y_{AD}) + (Y_{BC} + Y_{BD})} \tag{20}$$

$$Y_{cd} = \frac{(Y_{AC} + Y_{BC}) \cdot (Y_{AD} + Y_{BC})}{(Y_{AC} + Y_{BC}) + (Y_{AD} + Y_{BC})} \tag{21}$$

$$Y_{12} = \frac{Y_{AB} \cdot Y_{CD} - Y_{AD} \cdot Y_{BC}}{Y_{AC} + Y_{AD} + Y_{BC} + Y_{BD}} \tag{22}$$

As $Y_{ab}$ and $Y_{cd}$ are in parallel with $Y_{AB}$ and $Y_{CD}$, we can express them in

$$Y_1 = Y_{AB} + Y_{ab} \tag{23}$$

$$Y_2 = Y_{CD} + Y_{cd} \tag{24}$$

Using (20) to (24), we can illustrate the $\pi$-network model, as in Fig. 2(c). Based on [21], we can consider the two-port $\pi$-network model as a conformal transformation in the complex domain. In other words, if we consider the load admittance as a point on the complex domain $Y_L$-plane, the input admittance is a point on the complex domain $Y_{in}$-plane, then the two-port model maps the output plane onto the input plane or vice versa without changing the angles.

Fig. 3 illustrates the connection of the two-port network to a source and a load and the mapping between the input and the output complex planes. The input admittance ($Y_{in}$) is a conformal transformation of the load admittance to the input complex plane. In contrast, the two-port model maps the source admittance ($Y_s$) and the current source ($I_s$) to the output complex plane, as the output admittance ($Y_{out}$) and the output current source ($I_{out}$).

Thus, we can express the mapping as

$$Y_{in} = Y_1 - \frac{Y_{12}^2}{Y_2 + Y_L}, \tag{25}$$

$$Y_N = Y_{out} = Y_2 - \frac{Y_{12}^2}{Y_1 + Y_s} \tag{26}$$

$$i_N = \frac{Y_{12}}{Y_1 + Y_s} i_s \tag{27}$$

$$Y_{in} = Y_1 - \frac{Y_{12}^2}{Y_2 + Y_L}, \tag{28}$$

## IV. EXPERIMENTAL VERIFICATION

In the first step, we made a capacitor for verifying the fringing effect using two $150 \times 150$ mm aluminum plates insulated by covering them with a plastic lamination pouch. Using an Agilent 4285A LCR meter in the four-terminal pair measurement configuration, we measured the air-gapped admittance at a distance ranging from 10 mm to 500 mm. In the second step,
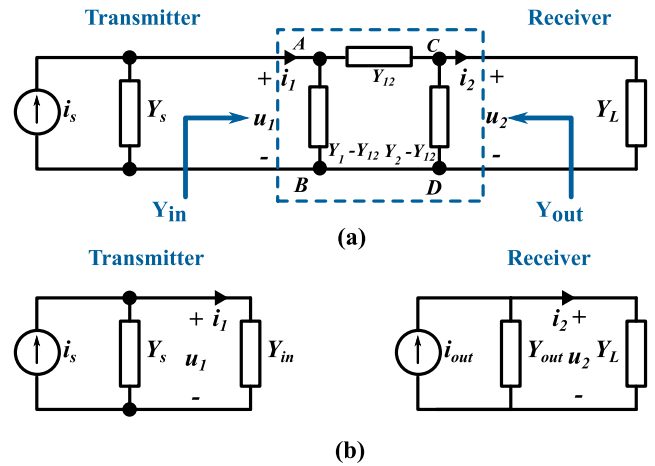


**FIGURE 3.** Model of source and a load connected to the *pi*-network: (a) *pi*-network connected to source and load. (b) The conformal transformation of admittance between transmitter and receiver sides [8].
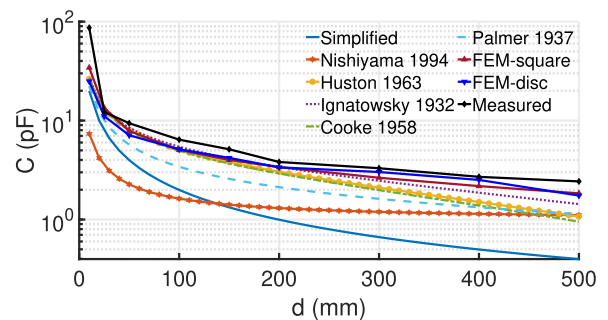


**FIGURE 4.** Comparison between the models listed in Table 1 and the measured capacitance as a function of separation distance in air.

we compared the measurements with the proposed analytical model, the models in Table 1, and the numerical model based on FEM using COMSOL Multiphysics. We used tap water as freshwater and collected seawater from the local harbor. In the last step, we tested a series compensated CPT system in seawater to examine the cross-coupling effect on the system's power transferability and efficiency.

### A. AIR-GAPPED CAPACITANCE
Fig. 4 shows a comparison between the models in Table 1, the FEM model, and the measured air-gapped capacitance at 100 kHz. The results, with an experimentally determined error that does not exceed 2 pF, show that the simplified model fails to predict the measurements. Fig. 5 explains the reason for the difference between the measured values and the ones based on the simplified model. It shows the electric field norm contours where the electric field is about 10 V/m at the edges of the plates. The fringing effect cannot be neglected for the air-gapped or submerged capacitor even when the aspect ratio (*b*) is small.

The FEM models for squared- and disc electrodes give approximately the same results, which shows that the approximation in (3) is valid. The maximum difference between the FEM-square and FEM-disc is 10 pF at 10 mm separation
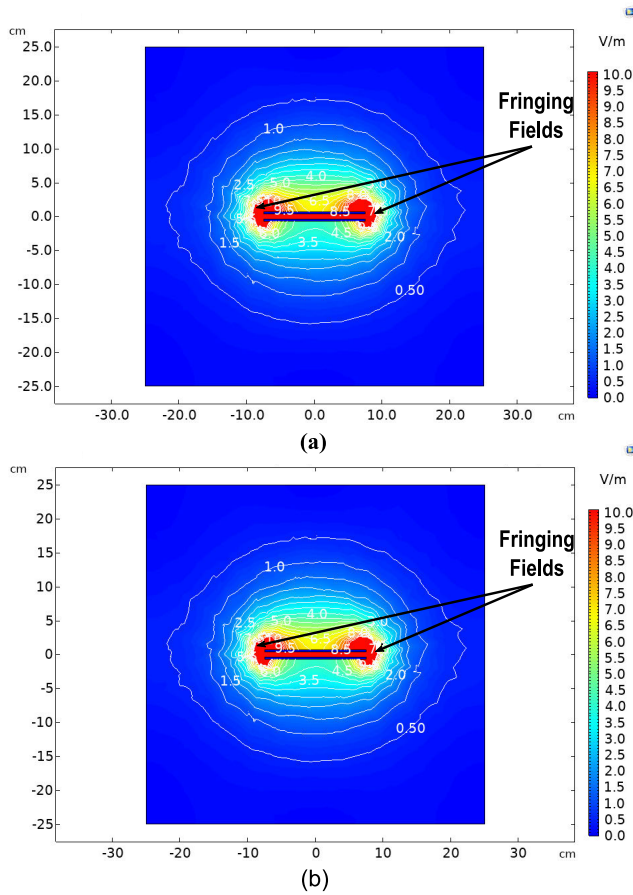
**FIGURE 5.** Fringing effect with aspect ratio b = 0.067: (a) Air-gapped capacitor. (b) Underwater capacitor.

distance, which we can attribute to the fields irregularities near the edges of the squared plate. The FEM models predict the measured values more accurately than the other models over the distance range. In contrast, the other models such as Palmer 1927, Ignatowsky 1932, Cooke 1958, and Huston 1963 can predict the measured values when the gap is in the range of 50 mm to 200 mm. These models can predict the measured capacitance more accurately when the aspect ratio b is tiny.

Fig. 6 illustrates the proposed analytical approach (conformal transformation model), the numerical approach (FEM), and the measured capacitance for the air-gapped capacitor. Using (15) the conformal transformation model predicts the measured capacitance better than the FEM analysis. The highest achieved capacitance is 37.9 pF at 10 mm distance, and it reduces exponentially with the increase of the gap to reach 3.4 pF at 500 mm. The percent error of the conformal transformation model is lower than that for FEM, as shown in Fig 7. The error for both models increases as the aspect ratio b approaches zero. The analytical approach must consider electrode thickness to reduce errors for small aspect ratios.

### B. WATER CAPACITANCE
Like the air-gapped capacitor, we investigated the proposed analytical model, the numerical model, and the measured
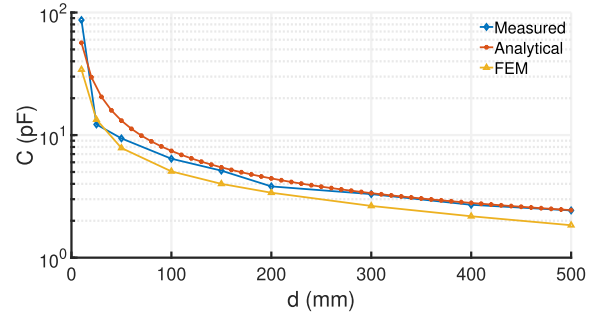


**FIGURE 6.** Comparison between the analytical approach, the numerical approach, and the measured capacitance of separation distance in air.
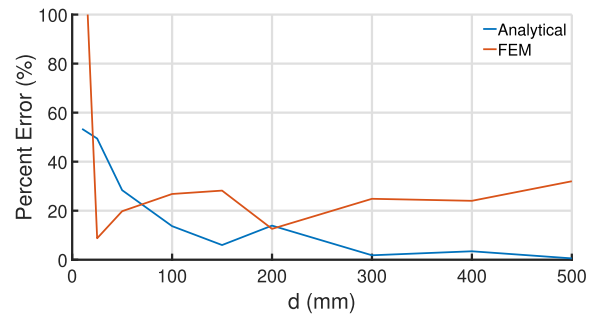


**FIGURE 7.** Percent error of the analytical and numerical approaches for the air-gapped capacitor.
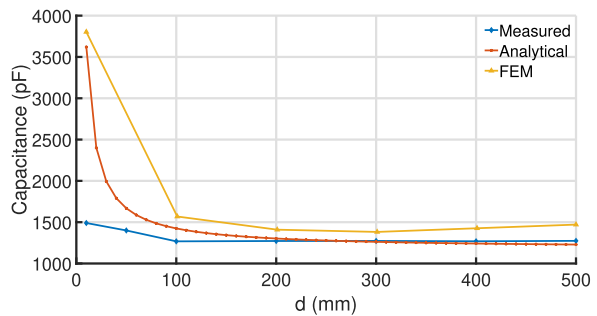


**FIGURE 8.** Comparison between the analytical approach, the numerical approach, and the measured capacitance of separation distance in water with $\kappa = 82$.

capacitance for the seawater capacitor. Fig 8 shows that using (18) the conformal transformation has a better prediction of the measured capacitance than the FEM analysis. However, both models fail to predict the measured values when the separation distance is 100 mm or lower. We can attribute this difference between the models and measured values at a short separation distance to the air bubbles that got trapped in the plastic lamination pouch.

The percent error of the conformal transformation model is lower than FEM for the submerged capacitor in seawater with 82 dielectric constant, as shown in Fig. 9. The plots show that the analytical approach predicts the capacitance in seawater more accurately than the FEM approach. The differences between the measured, the analytical, and the numerical values could be explained by different water characteristics, such
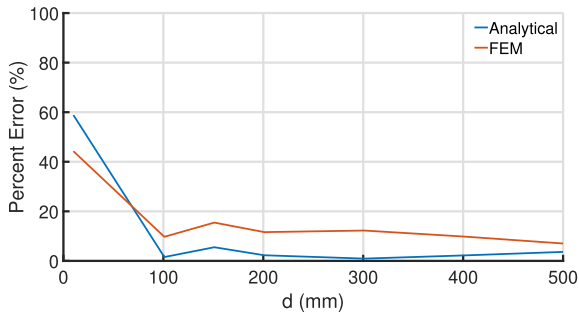
**FIGURE 9.** Percent error of the analytical and numerical approaches for the submerged capacitor.



**FIGURE 10.** Measured capacitance of air-gapped electrodes (dotted line), in freshwater electrodes (solid line), and in seawater electrodes (dashed line).
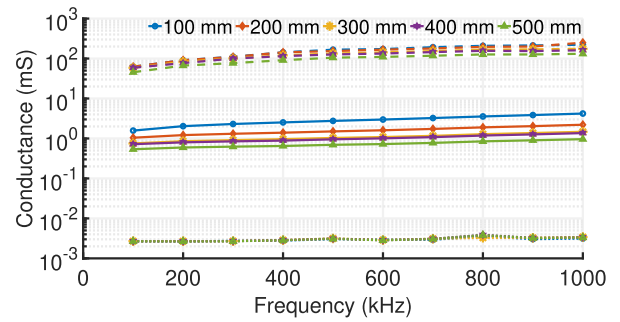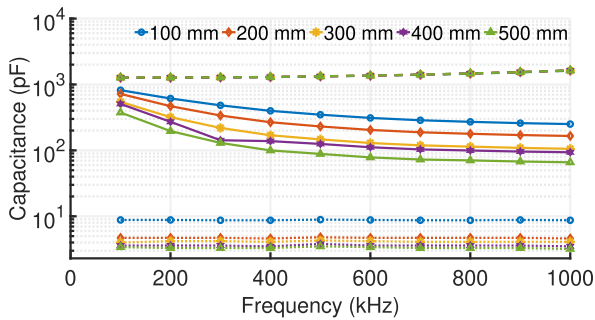


**FIGURE 11.** Measured conductance of air-gapped electrodes (dotted line), in freshwater (solid line), and in seawater electrodes (dashed line).



**FIGURE 12.** Converter topology.

as temperature and salinity. Both the analytical and numerical approaches can give a good approximation to the design of a CPT system.

## V. UNDERWATER CAPACITIVE CHARGING

The air-gapped capacitance range is much lower than those of the submerged in water, as shown in Fig.10. At 100 mm, the air-gapped capacitance decreases by only 0.1 pF when the frequency increases from 100 kHz to 1 MHz. The increase in the transfer distance has more effect on the capacitance. In contrast, the underwater capacitance can reach the nF range, which is about a thousand times higher than that of an air-gapped one. This high difference attributes to the presence of the water dipoles and the ions.

At 100 mm, the freshwater capacitance is about 819 pF at 100 kHz and decreases to 250 pF at 1 MHz. At the same separation distance, the under seawater capacitance is 1.3 nF at 1 MHz and increase to 1.6 nF at 1 MHz. The capacitance in freshwater is monotonically decreasing when the gap distance and frequency increase. In contrast, the capacitance in seawater slightly increases with increasing the frequency, and it does not significantly change with changing the transfer distance. We can attribute these differences between fresh- and seawater capacitance to the higher percentage of dissolved ions in the seawater than in freshwater.

The conductance of the air-gapped coupling is almost negligible compared to underwater coupling, as shown in Fig. 11. It is in the $\mu$S range and does not change with frequency
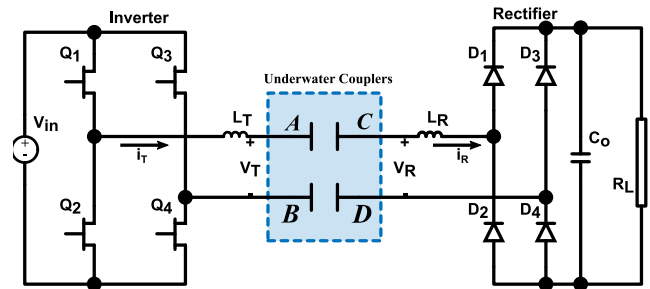
or distance, which we can attribute to the insulation characteristic of the air. Fig. 11 also shows that the conductance of the freshwater is about a hundred times lower than the one under seawater. Both the conductivity of the fresh- and seawater decrease with the separation distance and rise with the increase of the frequency.

From the above results, we continue testing the power transfer capability of the CPT system in seawater. Fig. 12 illustrates the converter topology we used to test underwater CPT. We used a four-plates structure by submerging four aluminum plates in the seawater. In addition, we utilized a GaN bridge inverter (Infineon EVAL1EDFG1HBGAN) and four Schottky diodes (C6D04065A) to build the rectifier bridge. The series L-compensation was chosen as a simple design that can provide electromagnetic interference (EMI) suppression. We set the switching frequency slightly higher than the resonant frequency to operate in the inductive mode and achieve soft-switching.

Using a single inductor in series at both transmitter and receiver sides, we can operate the CPT system in constant-current (CC) or constant-voltage (CV) modes through frequency splitting. It was chosen to operated the system in CC mode to achieve a zero-phase angle, aiming to cancel transferring reactive power, which is hard to achieve in CV mode. Table 2 lists the design parameters used in the experiment.

In a previous work [8], we showed that both the power transfer capability and the system's efficiency are a function of the admittance $Y_{12}$. Increasing the mutual capacitive coupling can enhance the power transfer capability and the system's efficiency. However, we notice from (20) that the

**TABLE 2.** Design parameters.

| Parameters | Values |
|---|---|
| Input voltage [V] | 250 |
| Operating frequency [MHz] | 1.1 |
| $L_T$ [µH] | 29.3 |
| $L_R$ [µH] | 30.9 |
| Plates' dimensions [mm×mm] | $150 \times 150$ |
| d [mm] | 300 |
| $d_p$ [mm] | 100 |
| Water's depth [mm] | 280 |



**(a)**



**(b)**
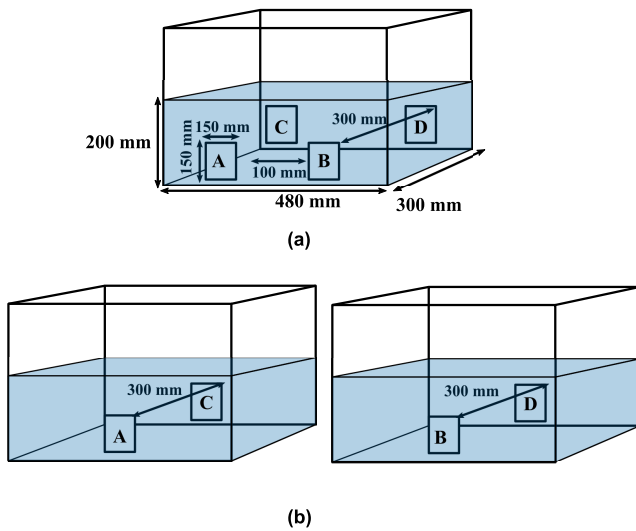
**FIGURE 13.** Experimental setups: (a) With the cross coupling effect. (b) Without the cross coupling.



**FIGURE 14.** With the cross coupling effect: the output voltage of the inverter (yellow), the current on the transmitter side $i_T$ (blue) the current on the receiver side $i_R$ (red), and the voltage across the couplers A and C (green).



**FIGURE 15.** Without the cross coupling effect: the output voltage of the inverter (yellow), the current on the transmitter side $i_T$ (blue) the current on the receiver side $i_R$ (red), and the voltage across the couplers A and C (green).

cross-coupling, $Y_{AD}$ and $Y_{BC}$, has a negative impact on the admittance $Y_{12}$ and hence the system's power transfer capability and the efficiency. To examine the influence of the cross-coupling, we submerged the four plates in a common container, as shown in Fig. 13(a). While neglecting the effect of the cross-coupling, we submerged the plates (A and C) and (B and D) in two different containers, as depicted in Fig. 13(b). In practice, we can increase the distance between plates A and B and C and D to eliminate the cross-coupling effect.

Firstly, when we submerged the plates in the same container, we achieved 14.7 W the output power with 41.9 % efficiency. Fig. 14 shows the currents on both the transmitter and the receiver sides and the voltage across the couplers A and C. The phase shifts between the currents and voltage indicate a high reactive power circulating in the system, which explains the system's low power and efficiency. The figure also shows that the switches $Q_1$ and $Q_4$ switched on when the transmitter side's current is negative, thus achieving a zero voltage switching (ZVS) condition. In addition, the results show that the current on the receiver side suffers from high harmonic contents, as shown in impure sinusoidal sine wave, which may result in EMI problems.
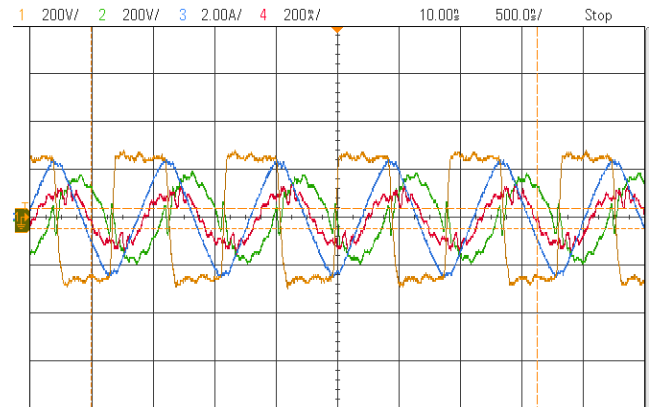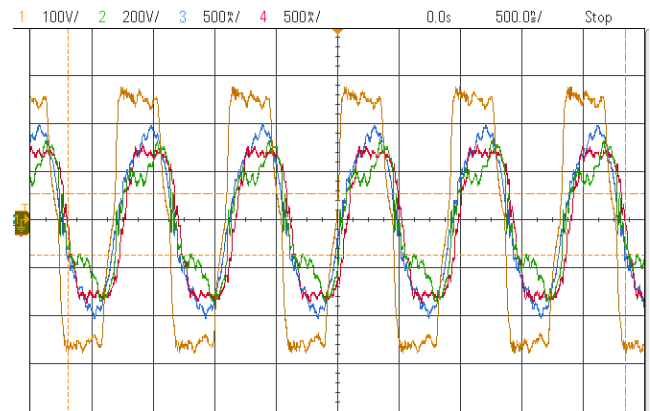
Secondly, we separated plates A and C from plates B and D to neglect the cross-coupling effect. Under the same design parameters, we achieved an output power of 129.2 W with about 81.2 % efficiency. Fig. 15 shows the currents and the voltages with a neglected cross-coupling case study. The phase shift between the current and voltage is small, which explains the system's high output power and good efficiency. Moreover, the result shows that the inverter achieved zero current switchings (ZCS), as the switching frequency is close to the CC mode frequency. As with the fringing, the harmonics problem increases in the current on the receiver side.

Fig. 16 shows the breakdown losses of the system with and without the effect of the cross-coupling. More than 90% of the losses are in the underwater capacitive coupling for both cases. We can attribute the losses to the water conductivity. The cross-coupling also increases the losses underwater resulting in low efficiency and less transfer power. Table 3 lists a comparison of this work with other underwater CPT systems in the literature in terms of compensation circuit, transfer power, system efficiency, operating frequency,

**TABLE 3.** Comparison between underwater CPT systems.

| Ref. | Compensation | Power (W) | Efficiency (%) | Frequency (MHz) | distance (mm) | size (mm) |
|------|--------------|-----------|----------------|-----------------|---------------|-----------|
| [9] | LC | 226.9 | 60.2 | 1 | 500 | $200 \times 200 \times 1$ |
| [11] | LC | 400 | 90 | 107.7 | 20 | $150 \times 205 \times 1.6$ |
| [12] | LCLC | 100 | 80.2 | 0.625 | 150 | $500 \times 500 \times 3$ |
| This work | L | 129 | 81.2 | 1.1 | 300 | $150 \times 150 \times 3$ |
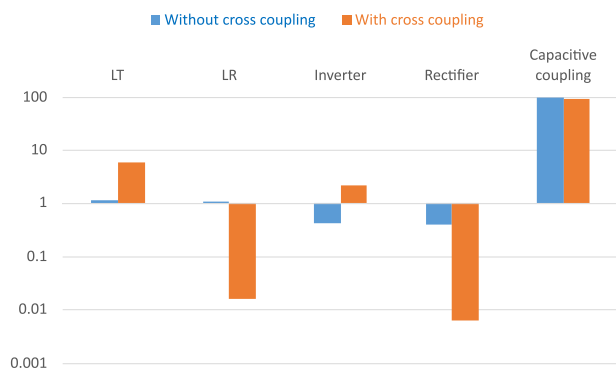


**FIGURE 16. Power loss breakdown: without the cross coupling effect and with the cross coupling effect.**

transfer distance, and coupler size. In this work, the underwater CPT system is smaller in size and simpler in compensation than the others and can achieve an efficiency of over 80% at 300 mm separation distance if we solve the problem of cross-coupling.

## VI. CONCLUSION

This paper investigated the fringing effect on the capacitance of both an air-gapped CPT system and an underwater CPT system. It proposes mathematical models to calculate the air-gapped and underwater capacitance using the conformal transformation and verified the models using FEM models in COMSOL and experimentally measured values. The proposed models showed improvements over previously proposed FEM and other analytical approaches. The paper also modeled the capacitive coupling using the two-port model and analyzed it as a conformal mapping transformation in the complex domain. The experimental measurements demonstrated that we can improve the coupling by submerging the coupling plates in seawater. The results also showed that changes in the gap distance and the operating frequency do not significantly affect the underwater coupling. Thus, the paper further examined the effect of cross-coupling on the underwater system's power transferability and efficiency and found that it can degrade the system's power transfer capability and efficiency. A system without cross-coupling effects can achieve an output power of 129 W with an efficiency of 81.2%.

## REFERENCES

[1] M. Z. Erel, K. C. Bayindir, M. T. Aydemir, S. K. Chaudhary, and J. M. Guerrero, "A comprehensive review on wireless capacitive power transfer technology: Fundamentals and applications," *IEEE Access*, vol. 10, pp. 3116–3143, 2022.

[2] A. Ahmad, M. S. Alam, and R. Chabaan, "A comprehensive review of wireless charging technologies for electric vehicles," *IEEE Trans. Transport. Electrific.*, vol. 4, no. 1, pp. 38–63, Mar. 2018. [Online]. Available: https://ieeexplore.ieee.org/document/8101562/

[3] G. A. Covic and J. T. Boys, "Modern trends in inductive power transfer for transportation applications," *IEEE J. Emerg. Sel. Topics Power Electron.*, vol. 1, no. 1, pp. 28–41, Mar. 2013.

[4] F. Lu, H. Zhang, and C. Mi, "A review on the recent development of capacitive wireless power transfer technology," *Energies*, vol. 10, no. 11, p. 1752, Nov. 2017.

[5] H. Zhang, F. Lu, H. Hofmann, W. Liu, and C. C. Mi, "A four-plate compact capacitive coupler design and LCL-compensated topology for capacitive power transfer in electric vehicle charging application," *IEEE Trans. Power Electron.*, vol. 31, no. 12, pp. 8541–8551, Dec. 2016.

[6] F. Lu, H. Zhang, and C. Mi, "A two-plate capacitive wireless power transfer system for electric vehicle charging applications," *IEEE Trans. Power Electron.*, vol. 33, no. 2, pp. 964–969, Feb. 2018.

[7] H. Mahdi, B. Hoff, and T. Ostrem, "Evaluation of capacitive power transfer for small vessels charging applications," in *Proc. IEEE 29th Int. Symp. Ind. Electron. (ISIE)*, Jun. 2020, pp. 1605–1610.

[8] H. Mahdi, B. Hoff, and T. Østrem, "Optimal solutions for underwater capacitive power transfer," *Sensors*, vol. 21, no. 24, p. 8233, Dec. 2021.

[9] H. Zhang and F. Lu, "Feasibility study of the high-power underwater capacitive wireless power transfer for the electric ship charging application," in *Proc. IEEE Electric Ship Technol. Symp. (ESTS)*, Aug. 2019, pp. 231–235.

[10] M. Tamura, Y. Naka, K. Murai, and T. Nakata, "Design of a capacitive wireless power transfer system for operation in fresh water," *IEEE Trans. Microw. Theory Techn.*, vol. 66, no. 12, pp. 5873–5884, Dec. 2018.

[11] M. Tamura, K. Murai, and M. Matsumoto, "Design of conductive coupler for underwater wireless power and data transfer," *IEEE Trans. Microw. Theory Techn.*, vol. 69, no. 1, pp. 1161–1175, Jan. 2021.

[12] L. Yang, M. Ju, and B. Zhang, "Bidirectional undersea capacitive wireless power transfer system," *IEEE Access*, vol. 7, pp. 121046–121054, 2019.

[13] N. Sakai, D. Itokazu, Y. Suzuki, S. Sakihara, and T. Ohira, "One-kilowatt capacitive power transfer via wheels of a compact electric vehicle," in *Proc. IEEE Wireless Power Transf. Conf. (WPTC)*, May 2016, pp. 16–18.

[14] K. Yi, "Capacitive coupling wireless power transfer with quasi-LLC resonant converter using electric vehicles' Windows," *Electronics*, vol. 9, no. 4, p. 676, Apr. 2020.

[15] J. Dai and D. C. Ludois, "Capacitive power transfer through a conformal bumper for electric vehicle charging," *IEEE J. Emerg. Sel. Topics Power Electron.*, vol. 4, no. 3, pp. 1015–1025, Sep. 2016.

[16] H. Zhang, F. Lu, H. Hofmann, W. Liu, and C. C. Mi, "Six-plate capacitive coupler to reduce electric field emission in large air-gap capacitive power transfer," *IEEE Trans. Power Electron.*, vol. 33, no. 1, pp. 665–675, Jan. 2018.

[17] H. B. Palmer, "The capacitance of a parallel-plate capacitor by the Schwartz-Christoffel transformation," *Trans. Amer. Inst. Elect. Eng.*, vol. 56, no. 3, pp. 363–366, Mar. 1937. [Online]. Available: http://ieeexplore.ieee.org/document/5057547/

[18] G. J. Sloggett, N. G. Barton, and S. J. Spencer, "Fringing fields in disc capacitors," *J. Phys. A, Math. Gen.*, vol. 19, no. 14, pp. 2725–2736, Oct. 1986.

[19] H. Nishiyama and M. Nakamura, "Form and capacitance of parallel-plate capacitors," *IEEE Trans. Compon., Packag., Manuf. Technol. A*, vol. 17, no. 3, pp. 477–484, Sep. 1994. [Online]. Available: http://ieeexplore.ieee.org/document/311759/

[20] T. A. Driscoll and L. N. Trefethen, *Schwarz-Christoffel Mapping*. Cambridge, U.K.: Cambridge Univ. Press, 2009.

[21] C. G. Montgomery, R. H. Dicke, and E. M. Purcell, *Principles of Microwave Circuits*. New York, NY, USA: McGraw-Hill, 1987.

**HUSSEIN MAHDI** (Graduate Student Member, IEEE) received the M.Sc. degree in electrical engineering from The Arctic University of Norway (UiT), in 2019, where he is currently pursuing the Ph.D. degree. He also works as a Graduate Research with the UiT. His research interests include resonant converters, soft switching, wireless power transfer, and power factor correction.



**BJARTE HOFF** (Senior Member, IEEE) received the B.S. degree in maritime electroautomation from Vestfold University College, Borre, Norway, in 2008, the M.Sc. degree in electrical engineering from Narvik University College, Narvik, Norway, in 2010, and the Ph.D. degree in electrical power engineering from the Norwegian University of Science and Technology (NTNU), in 2016.

He was certified as an electrician, in 2004. His research interests include power electronics with application within future energy systems and electric transport, two inspiring areas that are important for the transition to a sustainable future. The use of power conversion technology through power electronics and associated control algorithms is essential for renewable energy, electric transport, and energy storage. Charging of electric vehicles, maritime vessels, and aircrafts is combining all those research areas on both component and system level, representing an important element for the electric future.



**PÅL GUNNAR ELLINGSEN** received the M.S. degree in applied physics from the Norwegian University of Science and Technology (NTNU), in 2010, and the Ph.D. degree in physics (optics) from NTNU.

He is currently an Associate Professor at UiT–The Arctic University of Norway. He is also a part of several research projects related to remote sensing, satellite construction, marine sciences, and optical communication. His research interests include optics, polarimetry, spectroscopy, remote sensing, satellite technology, data management, and education.



**TROND ØSTREM** (Member, IEEE) was born in Kjollefjord, Norway, in August 1956. He received the M.S. degree in electrical engineering and the Ph.D. degree from Narvik University College, Narvik, in 2002 and 2007, respectively.

He is currently an Associate Professor at UiT–The Arctic University of Norway. His research interests include distributed generation, power electronics, power system stability, and electric transportation.

• • •